

A Recirculation Cell Approach for Hydrodynamic and Mass Transfer Modeling in Bubble Columns with and without Internals

Möller, F.; Dehmelt, T.; Schmidt, N.; Lau, Y. M.; Hampel, U.; Schubert, M.;

Originally published:

October 2019

Chemical Engineering Journal 383(2020), 123197

DOI: <https://doi.org/10.1016/j.cej.2019.123197>

Perma-Link to Publication Repository of HZDR:

<https://www.hzdr.de/publications/Publ-30189>

Release of the secondary publication
on the basis of the German Copyright Law § 38 Section 4.

CC BY-NC-ND

A Recirculation Cell Approach for Hydrodynamic and Mass Transfer Modeling in Bubble Columns with and without Internals

Felix Möller^{1,*}, Tom Dehmelt¹, Nicole Schmidt¹, Yuk Man Lau¹, Uwe Hampel^{1,2}, Markus Schubert¹

¹ Institute of Fluid Dynamics, Helmholtz-Zentrum Dresden-Rossendorf, Bautzner Landstr. 400, 01328 Dresden, Germany

² Chair of Imaging Techniques in Energy and Process Engineering, Technische Universität Dresden, 01062 Dresden, Germany

* Corresponding author

Abstract

An advanced recirculation cell model is proposed, which describes fluid dynamics and mass transfer in bubble columns with and without internals. The new model incorporates the cell approach of Shimizu et al. [*Chem. Eng. J.* **2000**, 78, 21-28.] with latest breakup and coalescence kernels. Additionally, the gas flow structure is divided according to the two-bubble class assignment with fast-rising large bubbles in the column center and descending small bubbles near the wall following the liquid circulation pattern within the column's cross-section. The effect of internals is considered dividing the column further into 'sub-columns' derived from the internals' radial profile, which physically refines the liquid circulation pattern. The model was validated with experimental data of Möller et al. [*Chem. Eng. Sci.* **2018**, 179,265-283; *Chem. Eng.*

Res. Des. **2018**, 134; *Chem. Eng. Sci.* **2019**] for narrow (0.1 m diameter) and pilot-scale (0.39 m diameter) columns, respectively, with and without internals operated up to the well-developed churn-turbulent flow regime. Predictions for bubble size distribution, total gas holdup, Sauter mean diameter as well as interfacial area and volumetric mass transfer coefficients agree well with the experiments.

Keywords

Bubble column, tube bundle internals, recirculation cell model, two-bubble class approach, hydrodynamics, mass transfer

1 Introduction

Bubble column reactors (BCRs) are widely applied apparatuses for a variety of multiphase reactions such as oxidations, hydrogenations, and wastewater treatment as well as for biotechnological processes [1–4]. BCRs have simple designs and operate without moving parts, which make them comparably cost-effective in terms of CAPEX and maintenance. Gas is typically dispersed at the bottom, while liquid is either fed in batch or continuous mode. Excellent mass and heat transfer performance can be reached at comparably low energy input [5,6]. Most of the reactions in BCRs are exothermic, thus, require appropriate heat removal to guarantee isothermal, stable and safe operation. To provide sufficient heat transfer area, dense vertical internal tube bundles are mostly installed in BCRs [7–12]. As an example, 210 kJ reaction heat per mole of converted CO is released in the Fischer-Tropsch synthesis – a process, which is currently experiencing a renaissance reflected by major industrial investments in its exploitation. To remove the reaction heat from the Fischer-Tropsch synthesis, between 20 and 40 % of the reactor’s cross-sectional area is typically covered by internals, which significantly impact the

hydrodynamics depending on the tube bundle design [13–22]. An accurate modeling of hydrodynamics and mass transfer in BCR with internals is still an open point.

Schlüter [11] categorized the available BCR models into reactor models and hydrodynamic models, whereas the latter can be turned into reactor models accounting for chemical species through considering their specific reaction kinetics. Hydrodynamic models comprise axial and radial dispersion models [21,23,24], circulation flow models [25–27], compartment and bubble class models [28–31] as well as cell models [32]. CFD approaches involve highest hydrodynamic complexity [33,34], however, shall not be further addressed here as the computational afford is too high.

Dispersion models commonly lump microscopic effects (Reynolds, grid, swarm, deformation and interfacial turbulence) and macroscopic effects (due to radial flow distribution, channeling, mal-distribution and dead zones, velocity profiles, inner circulation and wakes) with gross mixing parameters. The axial dispersion model (ADM) perceives any deviation from plug flow as longitudinal mixing quantified by axial dispersion coefficients of the respective phases. This model can be further refined by accounting for transverse mixing via radial dispersion coefficients. Zonal mixing can be considered further refining the column into compartments of characteristic dispersion. For example, liquid circulation can be accounted for by distinguishing a core zone with fast-rising large bubbles and a wall zone with descending small bubbles. The dispersion models are primarily used to describe the overall mixing behavior, while cell models based upon vertical column segmentation are preferably used to predict bubble size distributions and mass transfer coefficients. Here, each cell is considered as fully mixed and is connected via heat and mass transfer to the neighbor cells. The compartment mixing model and the cell model are described in detail below. In particular, their limitations to properly account for the effects of internals are discussed.

2 Fluid Dynamic Models Revisited

2.1 Convection-Diffusion Compartment Approaches

The research group of Professor Duduković proposed a compartment model (schematically shown in Figure 1) to describe the mixing behavior in different zones of bubble columns based on comprehensive flow analyses using computer-automated radioactive particle tracking [28,30,31,35,36].

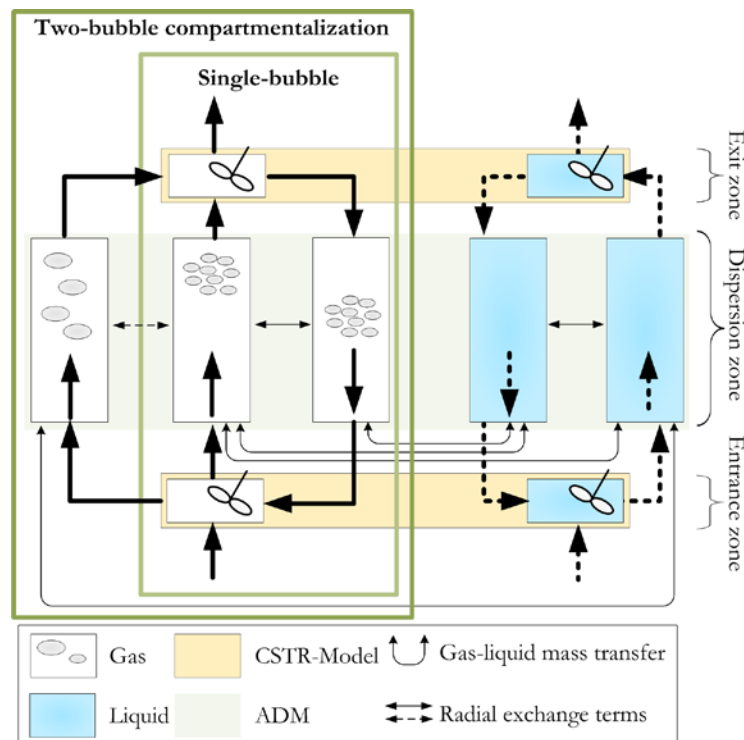


Figure 1: Schematic illustration of single- and two-bubble class compartment models.

Basically, gas and liquid phases are considered featuring individual circulation patterns. Gas and liquid rise in the column center (core) and descend near the wall. The model considers zones of different mixing characteristics described by respective axial dispersion coefficients ($D_{ax,1}$ and $D_{ax,2}$) in the respective convection-diffusion equations. Rising and descending gas and liquid are connected via exchange terms (D_{rr}). The convection-diffusion equations are solved for each

phase to predict the species concentrations. Although gas and liquid dispersions are known to differ significantly [37], Gupta et al. [28] assumed identical axial dispersion coefficients for both phases for simplicity reasons. The balance equations for gas and liquid phases are coupled via mass transfer terms specifically for up- and downflow of gas and liquid. All entrance and exit zones are considered as perfectly mixed and are described as continuous-stirred tank reactors (CSTR). The zone-specific mixing and the mass transfer parameters are commonly taken from empirical correlations which are obtained experimentally, for example via tracer response techniques and oxygen/nitrogen stripping, respectively. This model approach is also referred to as single-bubble approach as it is assuming mono-disperse bubbles.

Gupta et al. [28] further refined the model considering a bimodal BSD, also referred to as two-bubble class approach (TBCA). Here, large bubbles rise in the column center and small bubbles rise in their wakes and recirculate (descend) in the wall zone (Figure 1). Accordingly, a coupling term between small and large bubbles and a mass transfer coefficient to connect the convection-diffusion equations of large rising bubbles and ascending liquid are additionally required.

Coupling reaction kinetics with the convection-diffusion equations qualifies the model as a design tool for reactive bubble column processes. However, bubble characteristics and evolving BSDs cannot be obtained.

2.2 One-Dimensional Cell Model

Shimizu et al. [32] proposed a dynamic phenomenological 1D cell model, where the column of length L_c is divided into M cells of height $\Delta H = L_c/M$. In their model, changes in the bubble size, d_b , per time step, Δt , along their rise path are considered via breakup and coalescence kernels according to Prince and Blanch [38] (Figure 2). Further, only equal-sized breakup, spherical bubble shapes and ascending bubbles are assumed.

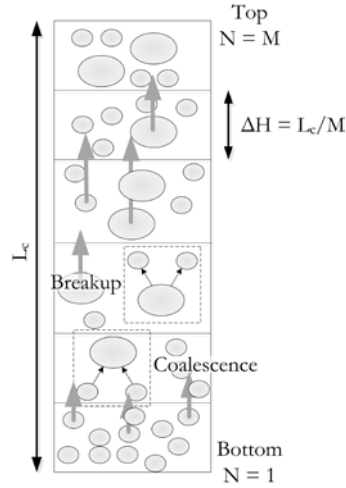


Figure 2: Schematic illustration of the cell model approach by Shimizu et al. [32]

The number of introduced mono-disperse gas bubbles depends on inlet gas flow rate and sparger design. Breakup and coalescence events occur simultaneously, however, only one event per bubble within Δt is allowed. Δt is the ‘observation time’ and can be chosen arbitrarily. However, it should not exceed the time required for the bubble breakup or coalescence event. Position and size for every bubble are calculated at every time step. The number of cells the bubbles are passing during Δt is

$$\Delta N = u_r' \frac{\Delta t}{\Delta H}, \quad (1)$$

while

$$N_{t+\Delta t} = N_t + \Delta N \quad (2)$$

is the subsequent bubble position at $t + \Delta t$. The actual bubble rise velocity, u_r' , is

$$u_r' = u_r + cu_1, \quad (3)$$

where u_r is the bubble rise velocity in quiescent liquid, that was defined by Lin et al. [39] according to

$$u_r = \left(2.14 \frac{\sigma_1}{\rho_1 d_b} + 0.505 g d_b \right)^{0.5}. \quad (4)$$

The recirculatory liquid flow structure is not explicitly considered. Instead, its damping effect on the average liquid velocity is approximated via $c = 2/3$ in Eq. 3.

At steady-state, Shimizu et al. [32] derived the BSDs for $M = 500$ and $\Delta t = 0.05$ s for column heights of 0.834 m and 1.7 m, respectively, at superficial gas velocities up to 0.03 m s^{-1} . Eventually, BSD data were utilized to calculate gas holdup, interfacial area and volumetric mass transfer coefficients (via penetration theory of Higbie [40]), which agreed reasonably well with predictions from literature correlations. However, recalling the uncertainties of the manifold from available correlations [41] experimental validation of the predicted BSD data is still due. The applicability of the cell model for churn-turbulent conditions and internals has to be verified, too. Some additional shortcomings of the cell model are:

- the liquid velocity profile is not considered when predicting the bubble rise velocities;
- the formation of only equal-sized daughter bubbles is assumed;
- the latest breakup and coalescence kernels are not yet implemented and tested;
- the bubble motion is restricted to ascending paths, and
- a constant inlet bubble size is considered for all studied velocities.

The cell model approach by Shimizu et al. [32] is used to predict mass transfer and the column performance. However, the model does not represent the flow pattern. Thus, a recirculation cell

approach is introduced below, which combines the cell approach by Shimizu et al. [32] with the bubble class assignment and the flow structures known from Gupta et al. [31]

3 Towards an Advanced Recirculation Cell Model

3.1 Conceptual Model Design

A recirculation cell model is proposed (Figure 3), which combines the TBCA according to the macroscopic flow structures (Section 2.1) and the axial cell division to account for breakup and coalescence (Section 2.2).

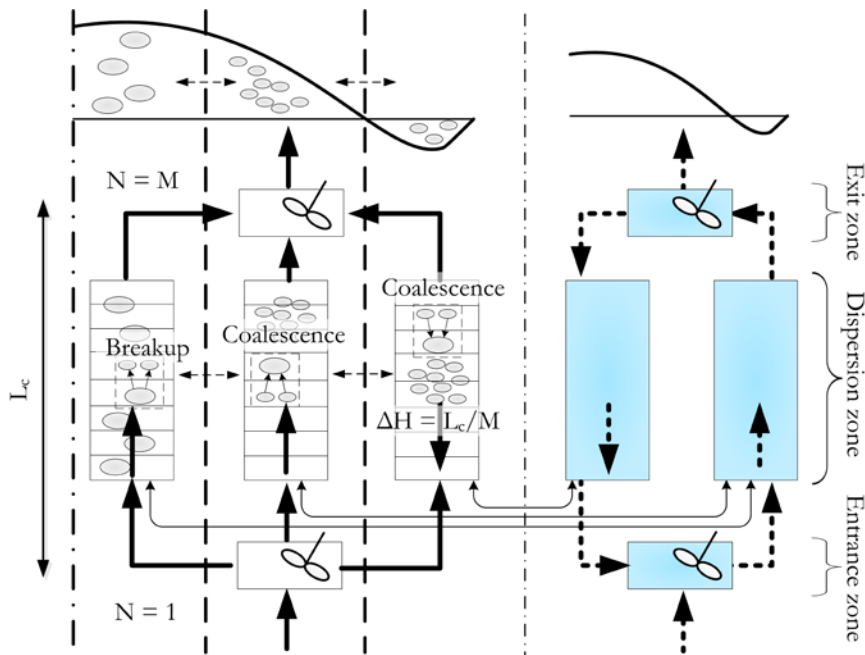


Figure 3: Schematic illustration of the recirculation cell model considering the TBCA.

The bubble motion is governed by the liquid velocity profile, which divides the BCR into zones of characteristic liquid flow behavior. A bubble size threshold is defined distinguishing rising and descending bubbles [22]. Furthermore, the column is axially divided into cells considering breakup and coalescence events, which eventually result in BSD changes along the column height.

The new model features latest breakup and coalescence kernels (see Appendix A.1 – A.2) as well as liquid velocity profiles for an appropriate consideration of the flow pattern.

The heat exchanger internals are considered in terms of solid profile or inversely as free area distribution, respectively, as shown in Figure 4.

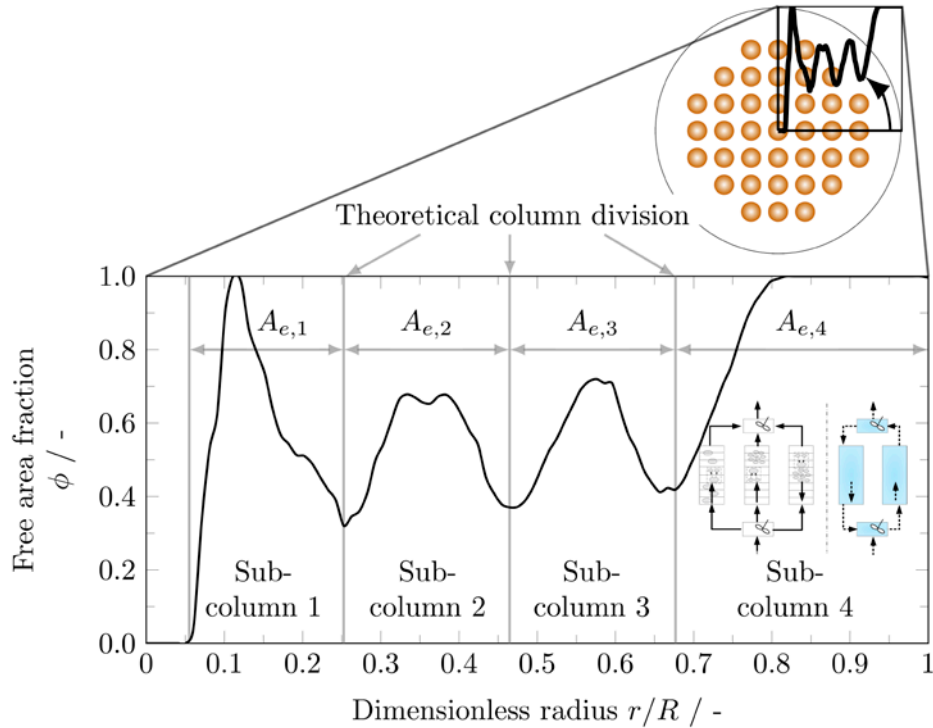


Figure 4: Division of the BCR into sub-columns based on the radial free area distribution. The lower peaks confine sub-columns with the cross-sectional area, $A_{e,i}$.

For the internals configuration shown in Figure 4, three lower peaks confine four zones (termed as sub-columns). Each sub-column features an individual liquid velocity profile. Further, two bubble classes with respective flow direction and velocities are considered in each sub-column. It should be noted that any exchange between different sub-columns is neglected and each sub-column is modeled separately. The details of the new model are explained below.

3.1.1 Definition of Gas Flow Structure and Bubble Allocation

For a proper consideration of the governing fluid dynamics, the bubbles are allocated within the column's cross-section according to their size. The actual bubble rise velocity is the summation of the bubble's rise velocity (Eq. 4) and the radial liquid velocity profile according to

$$u'_r(\xi) = u_r + u_1(\xi), \quad (5)$$

where ξ is the dimensionless column radius. Figure 5 shows a typical liquid velocity profile evolving in an empty BCR.

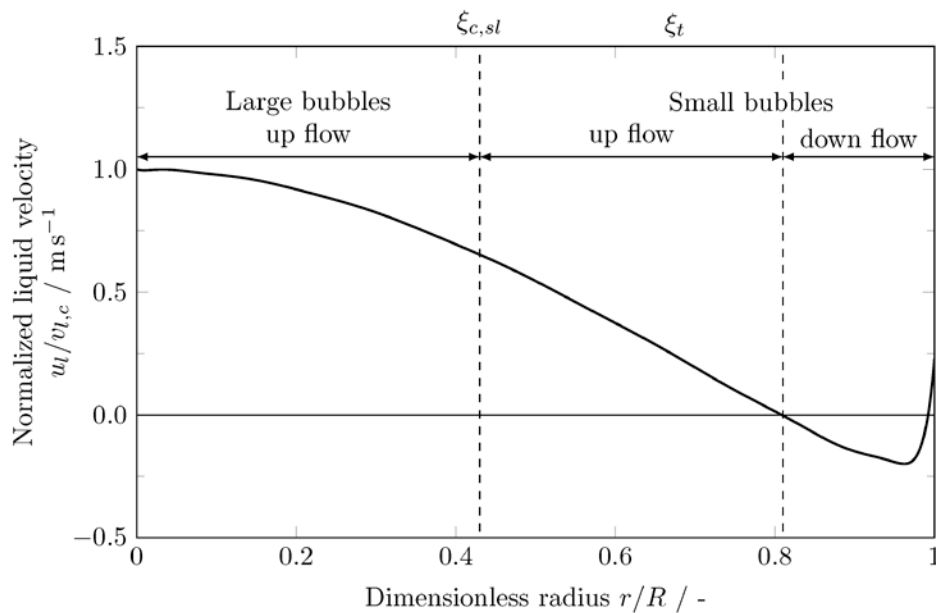


Figure 5: Time-averaged liquid velocity profile in a column without internals and division into zones of characteristic bubble size and flow direction.

While Gupta et al. [31] defined wall zone (descending small bubbles) and column zone (rising large bubbles and small bubbles in their wakes) only, the latter is now further refined into small and large bubbles rising at different radial positions depending on the liquid velocity in order to capture the rising small bubbles, which are typically dragged behind the wakes of the large

bubbles. A second transition point separating small and large rising bubbles is introduced for every cell at every time step according to their holdups

$$\frac{\varepsilon_{g,l}}{A_{c,l}} = \frac{\varepsilon_{g,su}}{A_{c,su}}, \quad (6)$$

where $A_{c,l}$ and $A_{c,su}$ are the areas occupied by large and small bubbles, respectively, and $\varepsilon_{g,l}$ and $\varepsilon_{g,su}$ are the holdups of large and small rising bubbles, respectively (see Figure 5). Replacing $A_{c,l}$ and $A_{c,su}$ with the dimensionless radius, $\xi_{c,sl}$ separates the core zones for every time step in every cell according to

$$\xi_{c,sl} = \xi_t \left(\frac{\varepsilon_{g,su}}{\varepsilon_{g,l}} + 1 \right)^{0.5}. \quad (7)$$

The transition point between up- and downflow, ξ_t , can be derived from the radial liquid velocity profile based on empirical correlations (Wu et al. [42]) or phenomenologically (Vitankar and Joshi [43]), assuming the radial gas holdup profile according to

$$\varepsilon_g = \frac{m+2}{m} (\bar{\varepsilon}_g - \varepsilon_w)(1 - \xi^m) + \varepsilon_w, \quad (8)$$

where ε_w is the gas wall holdup and $\bar{\varepsilon}_g$ is the total gas holdup. The liquid velocity profile can be calculated according to

$$\frac{du_l}{dr} = \xi R \frac{\tau_w}{\mu_t + \mu_l} \left[1 - \frac{R\rho_l g (\bar{\varepsilon}_g - \varepsilon_w)}{m\tau_w} (1 - \xi^m) \right], \quad (9)$$

with the boundary conditions

$$\frac{du_1}{dr} = 0 \text{ at } \xi = 0, \quad (10)$$

and

$$u_1 = 0 \text{ at } \xi = 1. \quad (11)$$

The parameters m and ε_w as well as turbulent viscosity, μ_t , and wall shear stress, τ_w , are chosen to comply with the continuity equation

$$\int_{r=0}^R 2\pi\varepsilon_1 u_1 r dr = \frac{\pi}{4} D^2 V_1. \quad (12)$$

The derivation of Eqs. 8 to 12 according to Vitankar and Joshi [43] is outlined in the Appendix A.3. It should be mentioned that the same procedure holds if internals are installed. Here, the column is divided into several sub-columns, featuring individual liquid velocity profiles (see Figure 6).

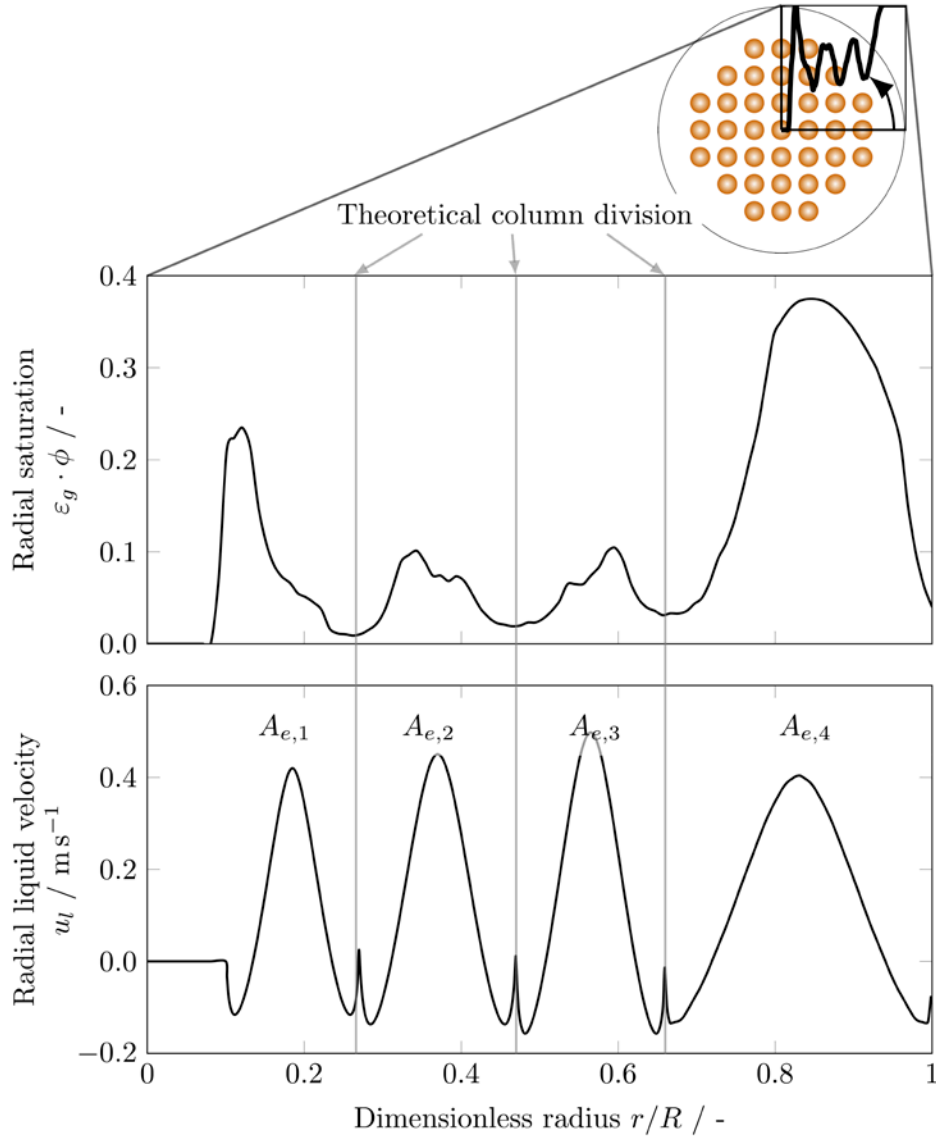


Figure 6: Schematic illustration of the mutually dependent profiles of gas saturation and liquid velocity.

To account for the available area (reduced by the internals), total and wall gas holdup in Eq. 9 are replaced by respective saturation values and fitted to the gas saturation profile (Figure 6, upper) according to

$$\frac{du_l}{dr} = \xi R \frac{\tau_w}{\mu_t + \mu_l} \left[1 - \frac{R\rho_l g (\bar{\beta}_g - \beta_w)}{m\tau_w} (1 - \xi^m) \right], \quad (13)$$

where

$$\bar{\beta}_g = \bar{\varepsilon}_g \phi \text{ and } \beta_w = \varepsilon_w \phi. \quad (14)$$

It should be noted that the radial holdup profile is multiplied by the free area fraction to ensure a parabolic holdup profile for each sub-column (see Figure 6, top). The parameters in Eq. 8 (ε_w , $\bar{\varepsilon}_g$ and m) are fitted to the gas saturation profile. For every sub-column, the holdup profile from the maximum (center of the respective sub-column) to the right-hand side minimum is considered. Upon parameters determination for every sub-column, the liquid velocity profile can be derived.

When there is no radial gas holdup data available, one can utilize the correlation of Wu et al. [42] to derive the liquid velocity profile according to

$$u_l = v_{l,c} \left(1 - 2.65n^{0.44}c \left(\frac{r}{R} \right)^{2.65n^{0.44}c} \right), \quad (15)$$

with

$$n = 2.188 \times 10^3 \text{Re}_g^{-0.598} \text{Fr}_g^{0.146} \text{Mo}_l^{-0.004}, \quad (16)$$

and

$$c = 4.32 \times 10^{-2} \text{Re}_g^{0.2492}. \quad (17)$$

The center-line liquid velocity for column or sub-column, $v_{l,c}$, can be calculated according to

$$v_{l,c} = 0.737 \left(u_g \sqrt{\frac{4\pi}{A_{e,i}}} \right)^{1/3} \quad (18)$$

or

$$v_{l,c} = 0.21 \left(g \sqrt{\frac{4\pi}{A_{e,i}}} \right)^{1/2} \left(\frac{u_g^3 \rho_l}{g \mu_l} \right)^{1/8}, \quad (19)$$

as proposed by Zehner [44] and Riquarts [45], respectively, which are valid for $D = 0.1 \dots 5.5$ m, $v_{l,c} = 0.2 \dots 1.1$ m s⁻¹ and $D = 0.138 \dots 0.6$ m, $u_g = 0.064 \dots 0.35$ m s⁻¹, respectively. It should be mentioned that the correlation of Wu et al. [46] was derived for a variety of gas and liquid properties and can be considered as reliable. The sub-column area, $A_{e,i}$, is separately determined for every column or sub-column, respectively.

It has to be noted that the bubbles can freely move within the columns cross-sections [47,48]. However, when internals are inserted, the column is further divided into sub-column, where a radial bubble exchange is neglected. Nevertheless, the bubbles can move radially within each sub-column.

3.1.2 Breakup and Coalescence Kernels

Liao [47] proposed a generalized bubble breakup and coalescence framework. The breakup frequency is defined as

$$\Omega = \begin{cases} \sum_k \left(\frac{\tau_k - \tau_c}{\rho_l} \right)^{0.5} \frac{1}{d_j} & (\tau_k > \tau_c) \\ 0 & (\tau_k < \tau_c). \end{cases} \quad (20)$$

The subscript k refers to the governing mechanisms leading to bubble breakup, namely, turbulence, laminar shear, eddy shear and interfacial slip. The breakup volume fraction, f_{bv} , is modeled as an M-shape distribution [49] instead of an equal-sized fraction as originally proposed.

The coalescence frequency is defined as

$$\Gamma(d_i, d_j) = \gamma(\Pi S_{ij,t} u_{r,t} \lambda_t + S_{ij,s} u_{r,s} \lambda_s + S_{ij,b} u_{r,b} \lambda_b + S_{ij,w} u_{r,w} \lambda_w + S_{ij,e} u_{r,e} \lambda_e). \quad (21)$$

The effect of the superficial gas velocity on the inlet bubble diameter is considered via the correlation of Jamialahmadi et al. [50] according to

$$d_b = d_o \left[\frac{5}{Bo^{1.08}} + \frac{9.261 Fr^{0.36}}{Ga^{0.39}} + 2.147 Fr^{0.51} \right], \quad (22)$$

where d_o is the sparger hole diameter, and Bo , Ga and Fr are dimensionless numbers to account for forces affecting the bubble formation. The correlation is valid for $\dot{V}_g = 0.1 \dots 10 \text{ cm}^3 \text{ s}^{-1}$, $\eta_l = 0.006 \dots 0.1 \text{ pa s}$ and $\sigma = 0.02 \dots 0.08 \text{ N m}^{-1}$.

3.2 Simulation Procedure and Parameter Extraction

Figure 7 shows the flowchart of the simulation procedure of the proposed model. Initially, parameters such as operational and geometrical parameters as well as drift flux constants are inserted, the number of sub-columns is determined and the liquid velocity profile is derived.

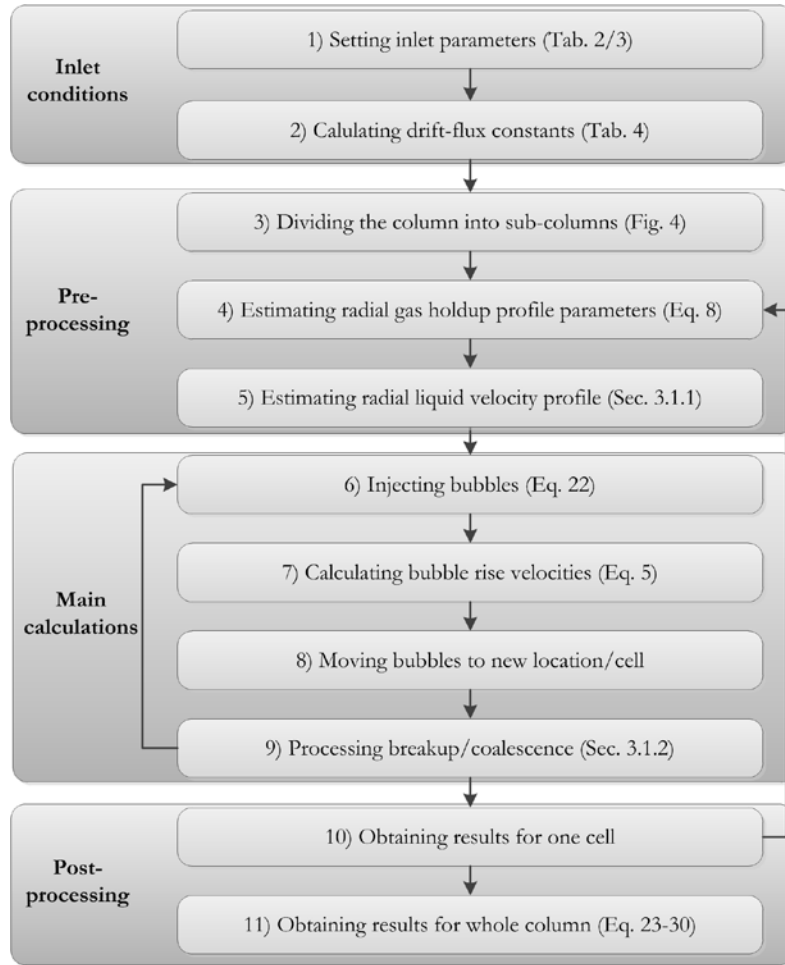


Figure 7: Flowchart of the simulation procedure of the advanced recirculation cell model for bubble columns with and without internals.

Subsequently, injected bubbles change their size due to coalescence and breakup and move depending on the macroscopic flow structures. Steps 4 to 10 are repeated until steady-state is reached. Eventually, the BSD is derived assigning the bubbles into 24 bins of 4×10^{-3} m size ranging from 0 to 0.1 m and gas holdup and Sauter mean diameter are determined assuming spherical bubbles according to

$$\varepsilon_g = \frac{V_g}{V_g + V_l} = \frac{\sum_i V_{bi}}{V_r}, \quad (23)$$

and

$$d_{32} = \frac{6\bar{V}_b}{\bar{S}_b}. \quad (24)$$

The interfacial area is defined as

$$a = \frac{6\varepsilon_g}{d_{32}}. \quad (25)$$

The liquid-side mass transfer coefficient is determined based on the penetration theory of Higbie [40] for the description of the unsteady-state mass transfer process around gas bubbles according to

$$k_l = \sqrt{\frac{4D_L}{\pi t_c}}, \quad (26)$$

where D_L is the molecular diffusivity and t_c is the gas-liquid contact time, which is typically defined as the ratio of bubble surface, S_B , to surface formation rate, R_{SF} ,

$$t_c = \frac{S_B}{R_{SF}}, \quad (27)$$

with

$$S_B = 4\pi \left(\frac{d_{32}}{2}\right)^2 \quad (28)$$

and

$$R_{SF} = \pi d_b u_b. \quad (29)$$

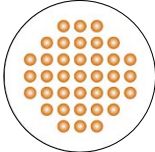
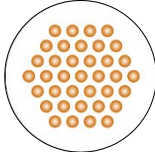
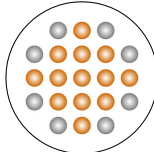
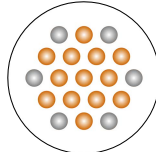
Eventually, the volumetric gas-liquid mass transfer coefficient is

$$k_1 a = k_1 \cdot a. \quad (30)$$

4 Validation Cases and Model Parameters

For model validation, BSD, gas holdup, Sauter mean diameter, interfacial area and volumetric mass transfer coefficients experimentally obtained for air/water bubble columns of different diameter (DN100 and DN400) with internals of various patterns and layouts [18,19,21,51,52] are considered. The configurations of internals and columns as well as fluid properties are summarized in Table 1 and Table 2, respectively. Relevant model parameters are summarized in Table 3.

Table 1: Patterns and layouts of the internals used (gray tubes hold for DN400 columns only).

Pattern					
	Square 8	Triangular 8	Square 13	Triangular 13	
	(s8)	(t8)	(s13)	(t13)	
DN100	d_o in $\times 10^{-3}$ m	8.0	8.0	13.0	13.0
	P in $\times 10^{-3}$ m	11.0	11.5	17.5	18.5

	d_h in $\times 10^{-3}$ m	7.6	5.6	11.8	8.9
	A_s in $\times 10^{-6}$ m ²	70.7	32.1	173.5	81.8
	A_c in %	24	24	23	23
	N	37	37	13	13
DN400	Type	Square 32 (s32)	Triangular 32 (t32)	Square 45 (s45)	Triangular 45 (t45)
	d_o in $\times 10^{-3}$ m	32.0	32.0	45.0	45.0
	P in $\times 10^{-3}$ m	42.9	45.9	61.3	64.3
	d_h in $\times 10^{-3}$ m	28.7	22.2	41.9	31.0
	A_s in $\times 10^{-6}$ m ²	1034.3	511.7	2161.1	995.6
	A_c in %	25	25	28	25
	N	37	37	21	19

Table 2: Column dimensions and fluid properties.

Parameter	DN100	DN400
Column diameter, D / m	0.10	0.392
Clear liquid height, L_c / m	1.1	2.65
Sparger hole size, $\times 10^{-3}$ m		0.5
Sparger opening area, %		0.14
Liquid (water) density, ρ_l / kg m ⁻³		997
Gas (air) density, ρ_g / kg m ⁻³		1.204
Liquid (water) surface tension, σ / N m ⁻¹		72.75×10^{-3}
Liquid (water) dynamic viscosity, η_l / Pa s		1×10^{-3}

Table 3: Model parameters.

Parameter	DN100	DN400
Smallest bubble diameter, $d_{b,\min}$ / m	0.5×10^{-3}	5×10^{-3}
Largest bubble diameter, $d_{b,\max}$ / m		0.1
Number of bubble classes, n_{class} / -		24
Initial film thickness, h_0 / m		1×10^{-4}
Critical film thickness, h_f / m		1×10^{-8}
Threshold to distinguish large and small bubbles, $d_{b,\text{lim}}$ / m		6×10^{-3}
Fraction of descending small bubbles, λ / -		0.5
Number of compartments, M / -	200	400
Lowest compartment of top zone, M_{top} / -	200	400
Highest compartment of sparger zone, M_{bottom} / -		5

The drift flux constants (see Eqs. A-30 and A-31 in Appendix A.3), summarized in Table 4 for calculating the liquid velocity profile according to Vitankar and Joshi [43], are derived from the slope of the total gas holdup as a function of the superficial gas velocity plots [18,51].

Table 4: Drift flux constant for the determination of the liquid velocity profile (see Eqs. A-29 to A-31).

	<i>DN100</i>					<i>DN400</i>				
Drift flux constant	<i>s8</i>	<i>t8</i>	<i>s13</i>	<i>t13</i>	<i>e100</i>	<i>s32</i>	<i>t32</i>	<i>s45</i>	<i>t45</i>	<i>e400</i>
C_0	2.03	1.85	2.31	1.77	2.34	3.30	3.17	3.11	3.67	3.84

C_1	0.33	0.46	0.34	0.43	0.30	0.32	0.50	0.75	0.27	0.37
-------	------	------	------	------	------	------	------	------	------	------

5 Model Validation

5.1 Results Obtained with a Phenomenological Liquid Velocity Profile

5.1.1 Gas Holdup

Experimental (symbols) and respective predicted data (connection lines are shown for clarity only) for the total gas holdup depending on the superficial gas velocity are shown in Figure 8 for DN100 (upper row) and DN400 (lower row). Line and symbol notions hold also for the other figures in this chapter.

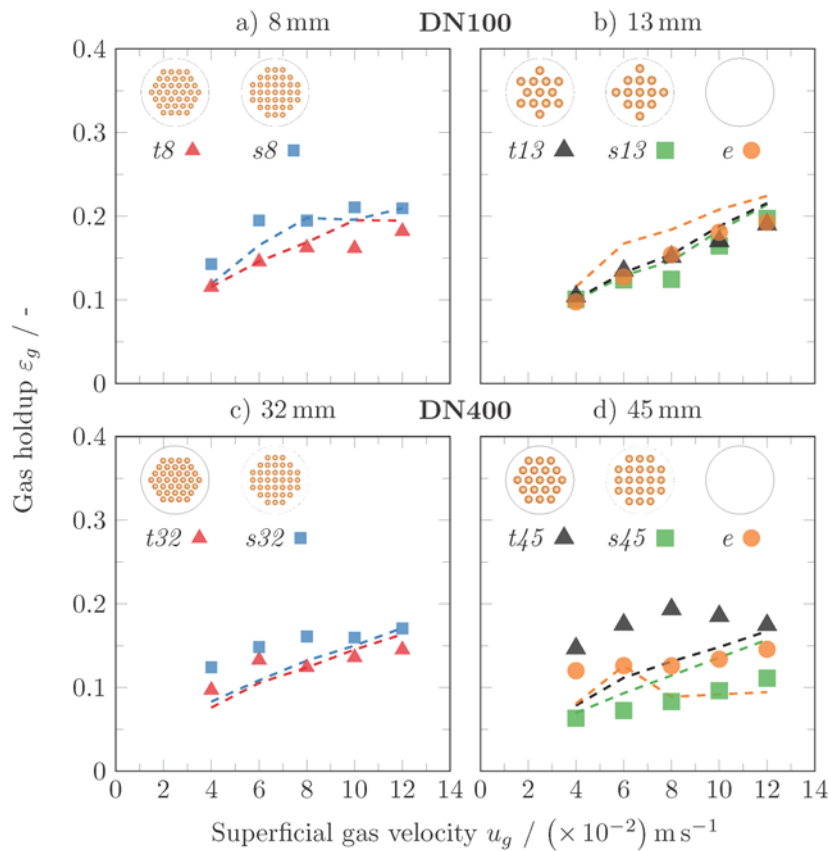


Figure 8: Comparison of experimental and predicted gas holdup data.

As evident from Figure 8, the holdup data for the narrow empty bubble column are overestimated, which is due to the larger turbulence level obtained by the breakup kernel of Liao [47]. Accordingly, the breakup frequency increases forcing the formation of small bubbles which causes higher holdup. The effect of internals is properly captured for the narrow columns as confirmed by the holdup curves (Figure 8, upper row). The predicted effect of the internals for the large column is less distinct. To capture the different tube sizes and patterns, the column was segmented and the liquid velocity profile was accordingly altered. However, the breakup frequency, which depends on the hydraulic sub-channel diameter, cannot be reproduced with the current model. This, in turn, leads to deviations between experiments and predictions. Highest gas holdups are obtained for the Triangular 45 (*#45*) configuration. The trend is properly met, however, the values still diverge from the experiments due to the high breakup frequency. Since the hydraulic sub-channel diameter determines bubble size, turbulence levels and breakup frequencies, further experimental or numerical studies are required to reliably relate breakup efficiency and hydraulic sub-channel diameter.

5.1.2 Bubble Characteristics and Mass Transfer

Bubble Size Distribution: Figure 9 summarizes the BSDs in terms of equivalent diameters ($d_e = (6V_b/\pi)^{0.33}$) for superficial gas velocities of 0.04ms^{-1} , 0.06ms^{-1} and 0.12ms^{-1} , corresponding to homogeneous, transition and churn-turbulent flow, respectively.

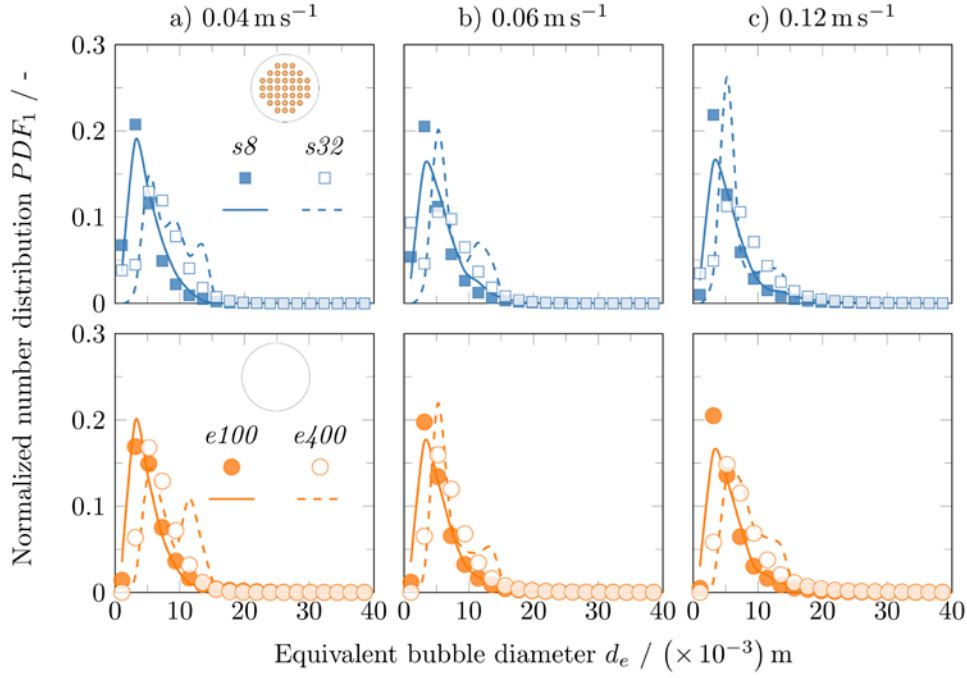


Figure 9: Measured (symbols) and predicted (lines) bubble size distribution for a) 0.04 m s^{-1} , b) 0.06 m s^{-1} and c) 0.12 m s^{-1} for square patterns (upper row) and the empty column (lower row).

As to be seen from Figure 9, the measured BSDs are properly reproduced by the proposed model. The flow structure in every sub-column is divided into large rising bubbles in the core and small descending bubbles in the wall region. This column sub-division accounts for local BSDs rather than only the axial evolution as considered in previous models. As confirmed by our previous studies [18,19,22,51], internals promote a higher breakup frequency, which is addressed by the small sub-columns in the model. Hence, the formation of large bubbles is suppressed.

With increasing column size the BSD widens, which is due to the bubble number that exponentially increases with increasing available area. Therefore, a larger bubble number obviously features a broader bubble diameter variance, which is accordingly predicted by the proposed model (see Figure 9).

Sauter Mean Diameter, Interfacial Area and Volumetric Mass Transfer Coefficient: The BSDs are further applied to derive bubble-specific parameters. Experimental and predicted data for Sauter mean diameter, interfacial area and volumetric mass transfer coefficient are compared by means of parity plots (Figure 9) for DN100 (solid symbols) and DN400 (empty symbols).

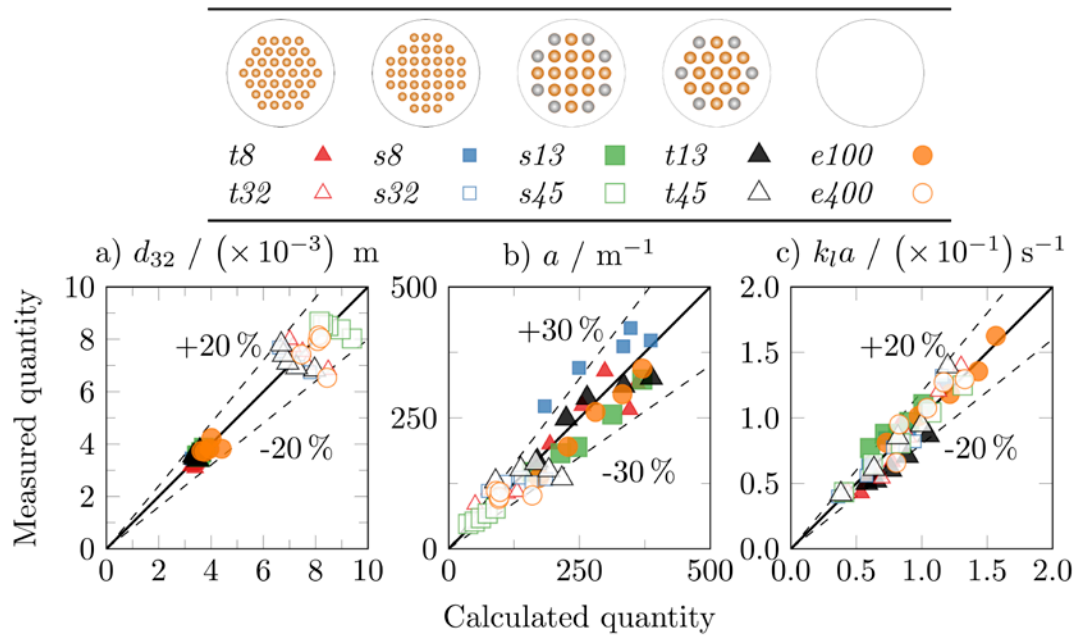


Figure 10: Sauter mean diameter, interfacial area and volumetric mass transfer coefficient parity plots for the narrow and pilot-scale column.

The predicted parameters are within a 30 % deviation band. The turbulence-dampening effect of the internals is properly reflected by the lower mass transfer rate compared to the empty column. The available space for the liquid eddy generation decreases with the addition of internals and the size of the sub-columns controls the turbulence level, e.g. larger sub-column feature higher turbulence levels and vice versa for smaller ones. Beyond the eddy size limitation and turbulence damping effect (to be implemented via sub-column's size restriction), proper modifications in the breakup kernels to account for different tube patterns is still required.

5.2 Results Obtained with Empirical Liquid Velocity Profiles

Contrary to the approach of Vitankar and Joshi [43], which relies on experimental data (gas holdup profile, drift-flux constants), the correlation of Wu et al. [42] for the liquid velocity profile (see Section 3.1.1) is applied here. The center-line liquid velocity is calculated according to correlations from Zehner [44] (Eq. 18) and Riquarts [45] (Eq. 19). In Figure 11, the obtained BSDs are compared with the phenomenological liquid velocity model of Vitankar and Joshi [43] (Eq. 9) for the square configurations ($s8$ and $s32$) from narrow and pilot-scale columns at superficial gas velocities of 0.04, 0.06 and 0.12 m s^{-1} .

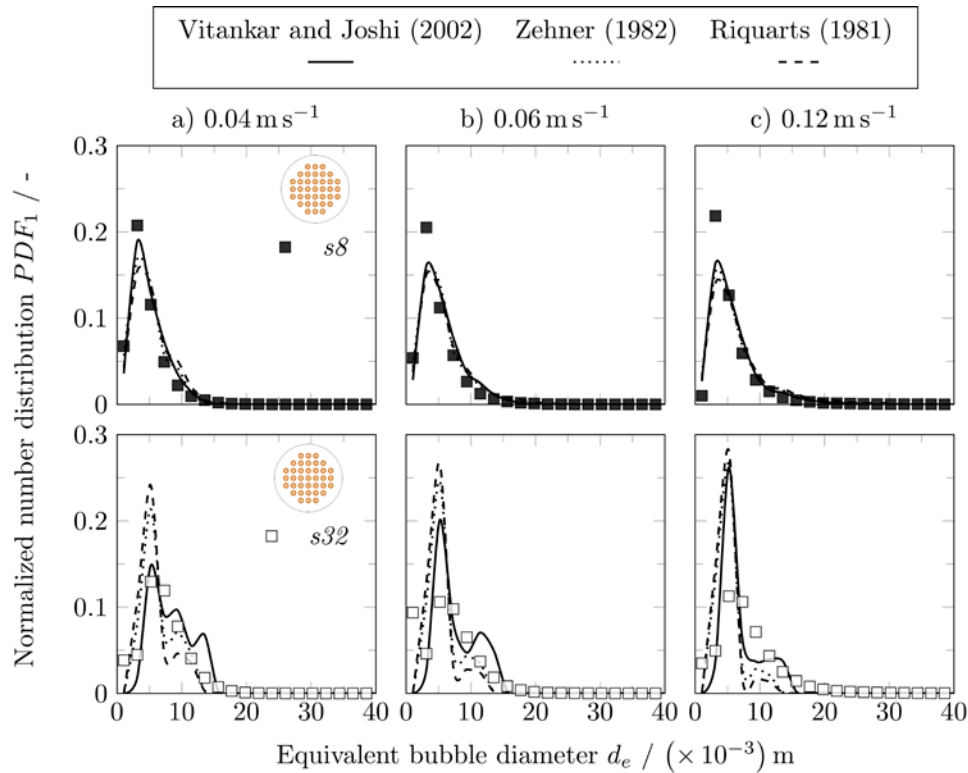


Figure 11: Bubble size distribution for Square 8 ($s8$, upper row) and Square 32 ($s32$, lower row) configurations for a) 0.04 m s^{-1} b) 0.06 m s^{-1} and c) 0.12 m s^{-1} using different approaches to determine the liquid velocity profile.

Best agreement with the measured BSD data is obtained determining the liquid velocity profile according to Vitankar and Joshi [43] using experimental input. Only minor differences occur for

the narrow column, while for the pilot-scale column, pronounced liquid velocity profiles have significant effects and the correlation of Zehner [44] returns least deviations from the experiments compared the results using Riquarts [45] correlation. The correlation of Zehner [44] calculates a larger liquid velocity with increasing column diameter (see Figure 11). Accordingly, the effect of the center-line liquid velocity on the BSD development is pronounced.

Subsequently, gas holdup, Sauter mean diameter, interfacial area, liquid-side and volumetric mass transfer coefficients have been determined based on the BSD results. Figure 12 shows the total holdup for Square 8 ($s8$) and Square 45 ($s45$) configurations based on the liquid velocity correlations. For the sake of comparison, the data for the approach of Vitankar and Joshi [43] based on the phenomenological velocity distribution are also included.

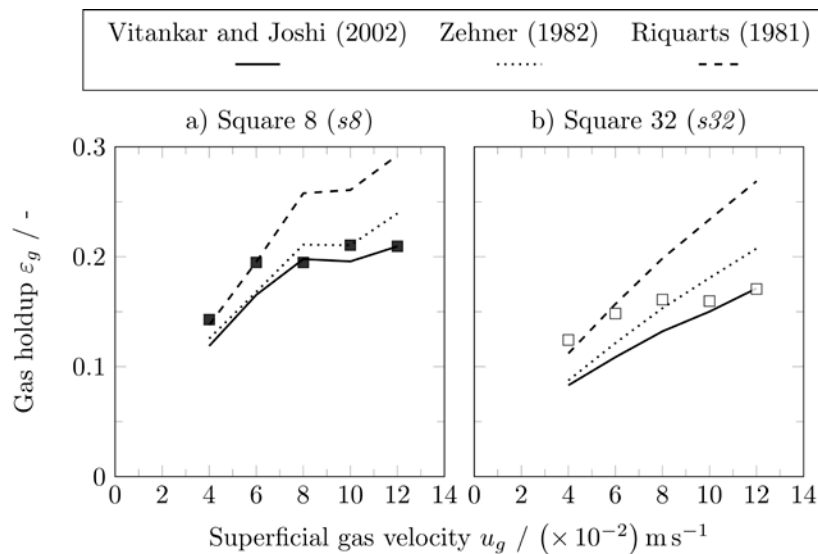


Figure 12: Gas holdup as a function of superficial gas velocity for a) Square 8 ($s8$) and b) Square 32 ($s32$) configurations using different approaches to determine the liquid velocity profile.

The approach to obtain the liquid velocity profile used in the model framework has a significant effect on the total gas holdup. It should be noted that the phenomenological model approach predicts better results than the empirical correlations. The center-line liquid velocity profile and,

hence, the bubble velocity is underestimated using the correlation of Riquarts [45]. Accordingly, the gas holdup in the column is overestimated caused by the higher bubble residence time. The correlation of Zehner [44] predicts a higher liquid velocity, which causes lower residence time and gas holdup. However, using the correlation of Zehner [44] within the model framework, the total gas holdup is fairly well predicted, when comparing the two empirical correlations.

Figure 13 shows Sauter mean diameter and interfacial area as a function of the superficial gas velocity.

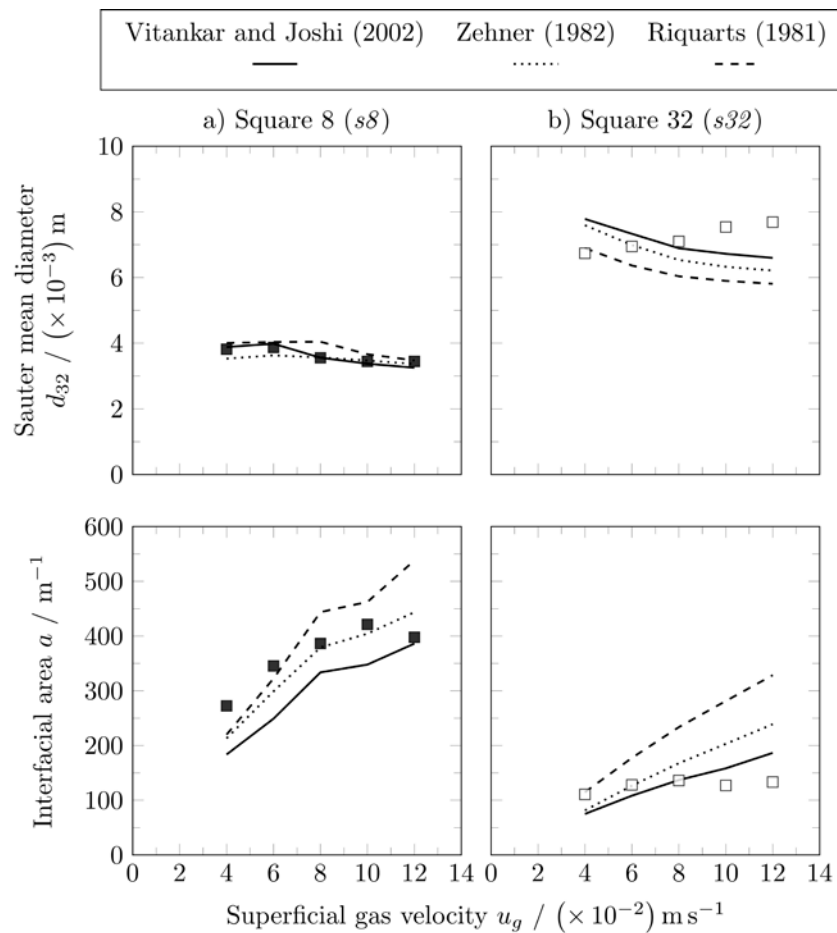


Figure 13: Sauter mean diameter (upper row) and interfacial area (lower row) as a function of superficial gas velocity for the a) Square 8 ($s8$) and the b) Square 32 ($s32$) configurations using different approaches to determine the liquid velocity profile.

The Sauter mean diameter decreases with increasing superficial gas velocity for the narrow column. The opposite trend is observed for the pilot-scale column, which is due to the stabilizing effect of the tube walls. The Sauter mean diameter for the narrow column is hardly sensitive for the center-line liquid velocity correlation within the model framework. For the pilot-scale column, the predictions show a decreasing Sauter mean diameter with increasing superficial gas velocity, which is opposite to the experiments. Wall stabilization effects of the tubes, which form one sub-channel, are not considered within the model framework, which leads to the oppositional prediction of a decreasing Sauter mean diameter. Accordingly, only liquid turbulence governs the course of the Sauter mean diameter as larger turbulence levels occur at higher superficial gas velocities, which leads to decreasing Sauter mean diameters. However, considering the correlations, the prediction of the Sauter mean diameter using the correlation of Zehner [44] is the most accurate one, which is due to faster rising bubbles. The same is observed for the interfacial area (Figure 13, lower row), where the application of the center-line liquid velocity correlation of Zehner [44] returns an acceptable agreement with the experimental data, while the interfacial area is over-predicted for the correlation of Riquarts [45]. However, using the phenomenological velocity profile model by Vitankar and Joshi [43], data prediction is superior compared to the correlations.

Figure 14 summarizes predicted and experimental mass transfer and the volumetric mass transfer coefficients for all velocity approaches.

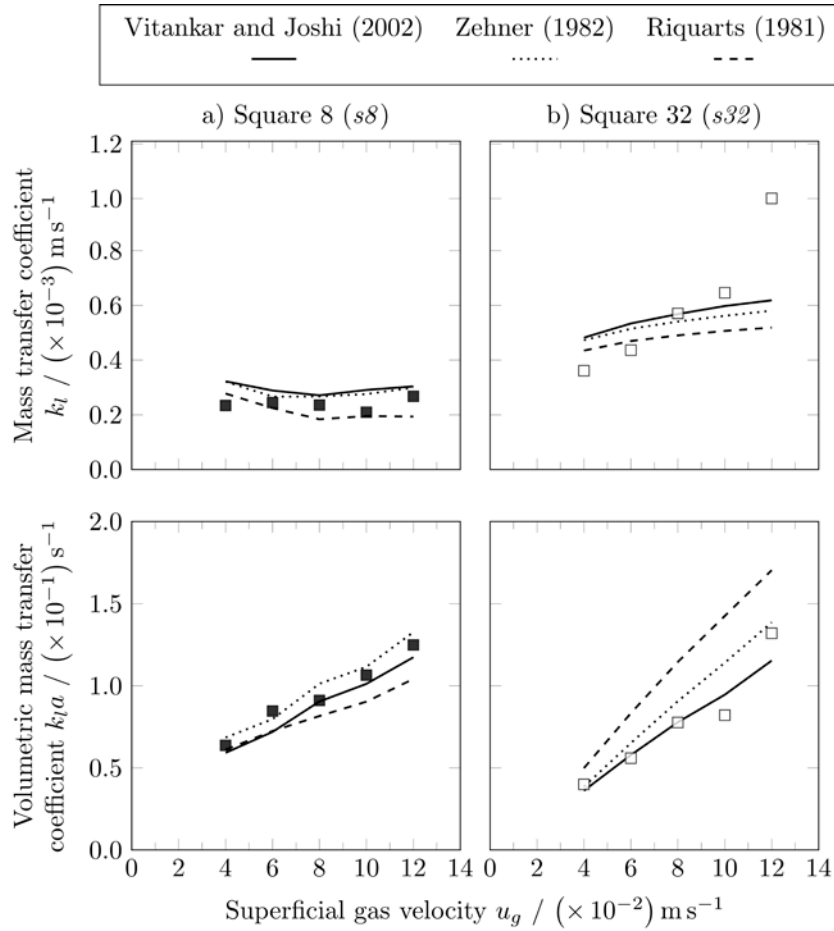


Figure 14: Liquid-side mass transfer coefficient as a function of superficial gas velocity for the a) Square 8 (*s8*) and the b) Square 32 (*s32*) configurations using different approaches to determine the liquid velocity profile.

The choice of the liquid velocity prediction within the model framework has a strong influence on the shear rate, which, in turn, affects the breakup and coalescence behavior (see Appendix A.1 – A.2) and, hence, liquid turbulence level and volumetric mass transfer coefficients. The effect for the pilot-scale column is pronounced, whereas it is almost negligible for the narrow column. This is due to the gas dispersion coefficient effect on the volumetric mass transfer determination, which exponentially increases with an increase of the column scale [53]. However, this effect is not considered using the penetration theory by Higbie [40]. Lower liquid velocity results in lower liquid turbulence levels and thus, lower mass transfer coefficients (correlation of Riquarts [45]) and vice versa (correlation of Zehner [44]). The correlation of Zehner [44] provides a proper velocity estimation, which leads to correct assignment of the liquid turbulence

level and, hence, a reliable description of the volumetric mass transfer has been obtained (see Figure 14, lower row).

Table 5 summarizes the deviation of the model predictions from the experimental data in terms of the average absolute relative errors (AARE) for the parameters described above.

Table 5: Summary of average absolute relative errors (AARE) of the various model approaches.

Parameter	Model considering the velocity profile according to					
	Vitankar and Joshi [43]		Zehner [44]		Riquarts [45]	
	<i>s8</i>	<i>s32</i>	<i>s8</i>	<i>s32</i>	<i>s8</i>	<i>s32</i>
ε_g	0.09	0.23	0.10	0.20	0.15	0.21
d_{32}	0.03	0.10	0.04	0.13	0.06	0.18
a	0.25	0.23	0.12	0.27	0.16	0.37
k_1	0.19	0.22	0.16	0.26	0.20	0.32
$k_1 a$	0.08	0.08	0.07	0.13	0.14	0.30
Global	0.13	0.17	0.10	0.20	0.14	0.28

From the AARE values it can be concluded that the model with the velocity profile obtained according to Zehner [44] provides almost equally good results as the phenomenological model proposed by Vitankar and Joshi [43]. Thus, in case of inaccessible experimental data for radial gas holdup and drift-flux coefficients, the calculation of the liquid velocity profile according to Wu et al. [42] considering the center-line liquid velocity correlation of Zehner [44] is recommended.

5.3 Literature Comparison

To assess the prediction capability of the proposed model and the model of Shimizu et al. [32], the predictions of the main hydrodynamic parameters are compared. It should be noted that only empty columns are considered to comply with the limitations of the model of Shimizu et al. [32]

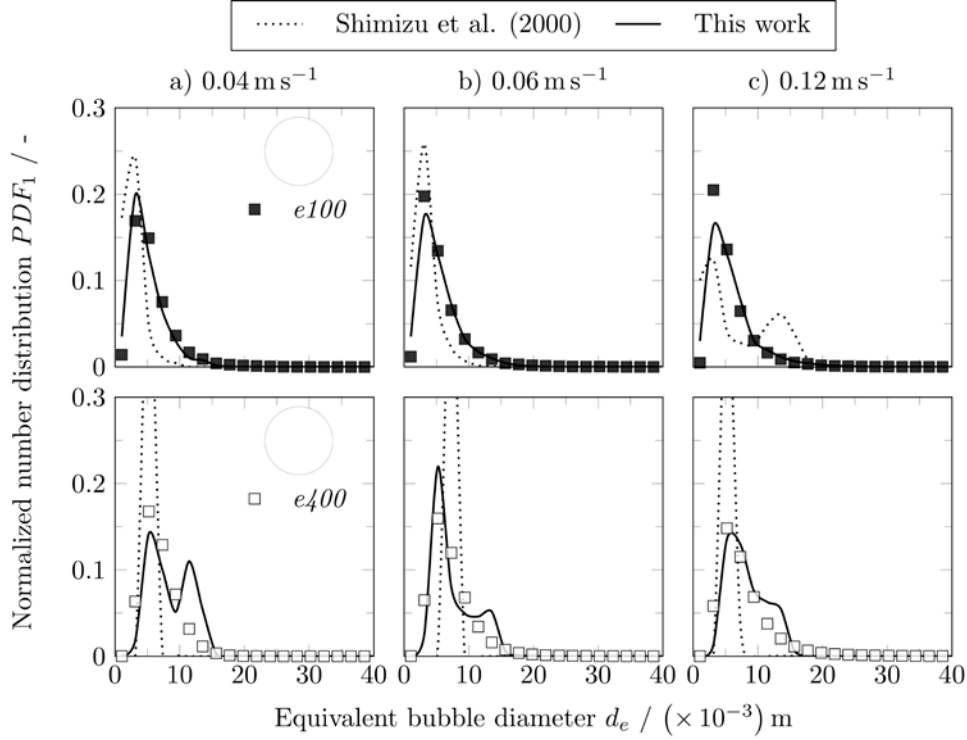


Figure 15: Bubble size distribution for the model proposed in this work and the model of Shimizu et al.[32][32] for DN100 (upper row) and DN400 (lower row).

Figure 15 illustrates that the model of Shimizu et al. [32] does not properly capture the BSDs, which is attributed to the simplified assumptions (e.g. equal sized bubble breakup, bubble up flow only, no radial bubble size distribution and incorrect liquid velocity profile), while the model proposed in this work fits very well, which can be attributed to the

- Definition of M-shaped daughter distribution in breakup kernels.

- Consideration of turbulence, laminar shear, eddy shear, interfacial slip, buoyancy and wake effects within the breakup and coalescence kernels.
- Incorporation of the second bubble class.
- Consideration of a more realistic liquid velocity profile.

Exemplarily, the model results are compared in terms of the Sauter mean diameter in Figure 16 (AARE values are provided as a quantifier of the model performance).

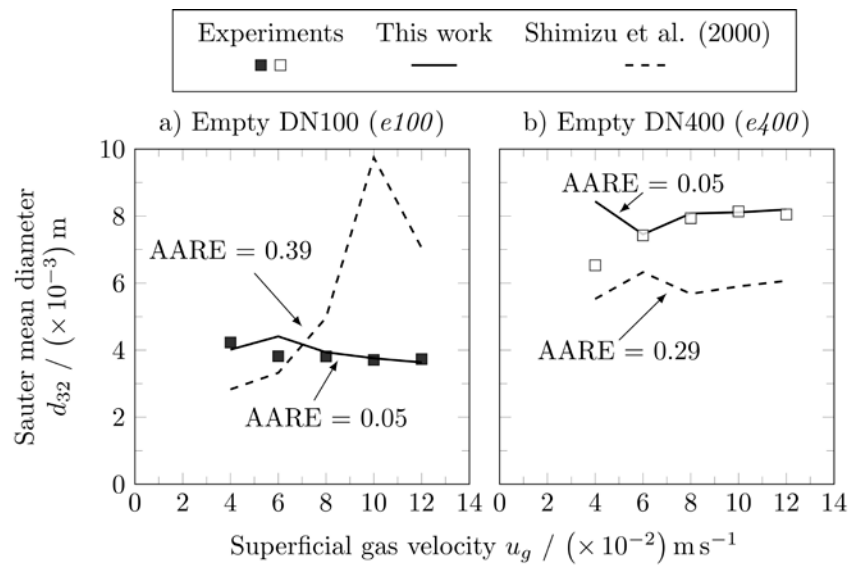


Figure 16: Sauter mean diameter predicted by the model of Shimizu et al. [32] and by the model proposed in this work for the empty bubble column.

The model of Shimizu et al. [32] fails to correctly predict the course of the Sauter mean diameter in particular at higher superficial gas velocities ($u_g > 0.07 \text{ms}^{-1}$). The two peaks of the BDS of the narrow column (Figure 15c, upper row) eventually cause much higher Sauter mean diameters (Figure 16). The AARE values of the corresponding hydrodynamic parameters are compiled in Figure 17.

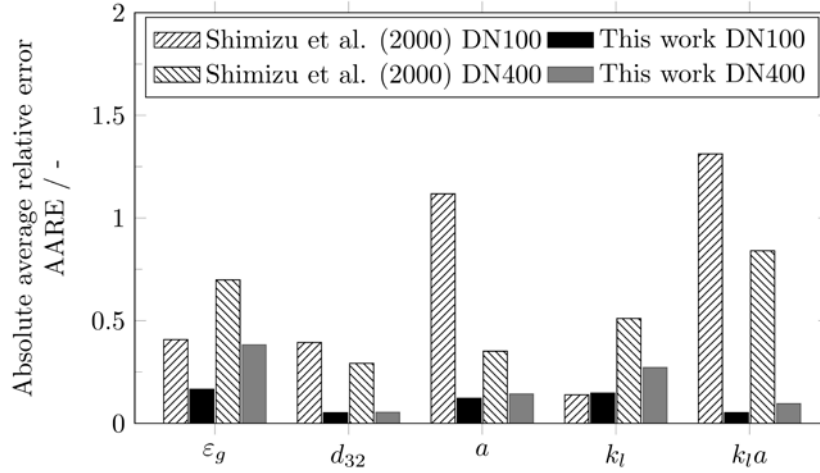


Figure 17: Comparison of the model of Shimizu et al. [32] and the model proposed in this work for all predicted fluid dynamic parameters.

The AARE values illustrate the superior prediction performance of the proposed model compared to the model of Shimizu et al. [32]. The main model improvements are the more realistic horizontal assignments of small and large bubbles as well as the proper consideration of the flow pattern in terms of the liquid velocity profile. The liquid velocity profile, which is used in the model framework, has the most significant effect on the overall model performance. Large liquid velocities lead to higher liquid turbulence levels, which forces higher bubble breakup and, hence, governs the respective fluid dynamic parameters. Furthermore, Shimizu et al. [32] considered only the turbulent kinetic energy of bombarding eddies as possible breakup mechanism, which leads to deviating BSDs and, hence, to deviating total holdup, Sauter mean diameter and interfacial area.

6 Conclusions

In this work, the phenomenological model of Shimizu et al. [32] was modified and adapted to predict hydrodynamic data for BCRs with dense internals for the first time. An axial compartmentalization based on the tubes' solid distribution was proposed to properly predict the

main hydrodynamic parameters. The formulation of the model using only algebraic equations instead of integrals drastically enhanced the computational effort.

The implementation of the coalescence and breakup kernels developed by Liao [47] resulted in a successful agreement with the experimental BSD values and, thus, a reliable prediction of associated parameters such as Sauter mean diameter, interfacial area, mass transfer and gas holdup.

Two methods for the determination of the liquid velocity profile have been implemented. One of which requires the experimental input of the radial gas fraction, whereas the other one is purely empirical. Slightly better results are obtained using experimental data for the gas holdup profile, however, a priori knowledge of the gas holdup profile is not necessarily required. The simulations revealed that column diameter and liquid velocity profile are the most crucial parameters within the model framework. The liquid velocity determines the bubble motion and bubble residence time as well as liquid turbulence level and breakup frequency, which increase with increasing column scale.

Acknowledgement

The authors gratefully acknowledge the European Research Council (ERC StG, No. 307360) for financial support.

Nomenclature

Abbreviations

ADM	Axial dispersion model
BCR	Bubble column reactor
BSD	Bubble size distribution

CSTR	Continuous-stirred tank reactor
TBCA	Two-bubble class approach

Latin symbols

A_c	Tube coverage, %
$A_{c,l}$	Large bubble area, m ²
$A_{c,su}$	Small rising bubble area, m ²
$A_{e,i}$	Equivalent sub-column area, m ²
A_s	Sub-channel area, m ²
a	Interfacial area, m ⁻¹
C_0	Drift flux constant, -
C_1	Drift flux constant, -
C_{35}	Coefficient, -
C_D	Drag coefficient, -
c	Constant for the local liquid velocity, -
c_{fbv}	Auxiliary variable for the breakup fraction, -
D	Column diameter, m
D_L	Molecular diffusivity, m ² s ⁻¹
d_{32}	Sauter mean diameter, m
d_b	Bubble diameter, m
d_c	Critical bubble diameter for the wake entrainment, m
d_e	Equivalent bubble diameter, m
d_i	Mother bubble for breakup and daughter bubble for coalescence, m
d_j	Daughter bubble for breakup and mother bubble for coalescence, m

d_o	Outer tube diameter, m
d_h	Hydraulic sub-channel diameter, m
f_{bv}	Breakage volume fraction, -
g	Gravitational constant, $m\ s^{-2}$
h_0	Initial film thickness, m
h_f	Critical film thickness, m
k_l	Liquid-side mass transfer coefficient, $m\ s^{-1}$
$k_1 a$	Volumetric mass transfer coefficient, s^{-1}
L_c	Clear liquid height, m
L_D	Dynamic liquid height, m
N	Number of tubes and number of compartments, -
M	Top compartment/total number of stages, -
P	Tube pitch, m
R_{SF}	Surface renewal rate, $m^2\ s^{-1}$
S_i	Surface, m^2
t	Time, s
t_c	Contact time, s
u_l	Local liquid velocity, $m\ s^{-1}$
u_g	Superficial gas velocity, $m\ s^{-1}$
u_r	Bubble rise velocity in quiescent liquid, $m\ s^{-1}$
u'_r	Actual bubble rise velocity, $m\ s^{-1}$
V_b	Bubble volume, m^3
V_i	Volumetric flow rate, $m^3\ s^{-1}$
$v_{l,c}$	Center-line liquid velocity, $m\ s^{-1}$
X	Iteration variable to close the liquid velocity profile, -

Dimensionless numbers

Bo	Bond number, $\frac{\rho_l g D^2}{\sigma}$
$Eö$	Eötvös number, $\frac{g(\rho_l - \rho_g)}{\sigma}$
Fr	Froude number, $\frac{u_g^2}{Dg}$
Ga	Galileo number, $\frac{\rho_l^2 D^3 g}{\mu_l}$
Mo	Morton number, $\frac{g \mu_l^4}{(\rho_l - \rho_g) \sigma^3}$
Re	Reynolds number, $\frac{D u_g (\rho_l - \rho_g)}{\mu_l}$

Greek Symbols

β_g	Gas saturation profile, -
ε_i	Gas (g) or liquid (l) holdup, -
ε_d	Turbulent energy dissipation, $m^2 s^{-3}$
ΔH	Compartment height, -
ΔN	Number of compartments a bubble passes during Δt , -
$\Delta N_{t+\Delta t}$	Compartment location of a bubble at next time step, -
Δt	Simulation time step, s
η_k	Kolmogorov length scale,
Γ	Coalescence frequency, s^{-1}
γ	Modification factor, -
$\dot{\gamma}$	Shear rate, s^{-1}
Π	Turbulent modification factor, -
ν_i	Kinematic viscosity, $m^2 s^{-1}$

λ_i	Coalescence efficiency, -
Ω	Breakup frequency, s^{-1}
Φ	Free area distribution, -
ρ_i	Gas (g) or liquid (l) density, $kg\ m^{-3}$
σ	Surface tension, $N\ m^{-1}$
τ_i	Stress, $N\ m^{-2}$
ξ	Dimensionless radial coordinate, -
$\xi_{c,sl}$	Dimensionless radial coordinate to separate small and large bubbles in the core zone, -
ξ_t	Dimensionless radial coordinate for up- and downflow transition, -

Subscripts

b	Bouyancy
c	Critical
e	Eddy
g	Gas
k	Destroying
l	Liquid
s	Shear
su	Small bubbles up flow
t	Turbulent
w	Wake

Bibliography

- [1] W.D. Deckwer, *Bubble Column Reactors*, (John Wiley & Sons Inc: 1992).

- [2] W.-D. Deckwer, R. Burckhart, G. Zoll, Mixing and mass transfer in tall bubble columns, *Chemical Engineering Science* 29 (1974) 2177–2188
- [3] Y.T. Shah, B.G. Kelkar, S.P. Godbole, W.-D. Deckwer, Design parameters estimations for bubble column reactors, *AIChE Journal* 28 (1982) 353–379
- [4] R. Badura, W.-D. Deckwer, H.-J. Warnecke, H. Langemann, Durchmischung in Blasensäulen, *Chemie Ingenieur Technik* 46 (1974) 399–399
- [5] W.-D. Deckwer, A. Schumpe, Improved tools for bubble column reactor design and scale-up, *Chemical Engineering Science* 48 (1993) 889–911
- [6] A. Schumpe, A.K. Saxena, L.K. Fang, Gas/liquid mass transfer in a slurry bubble column, *Chemical Engineering Science* 42 (1987) 1787–1796
- [7] F. Hugues, B. Szymkowiak, J.C. Viguie, J.M. Schweitzer, M. Munier, D. Chretien, E. Caprani, D. Douziech, Internal exchanger for gas-liquid-solid reactor for fischer-tropsch synthesis, (2010)
- [8] C. Maretto, V. Piccolo, J.C. Viguie, G. Ferschneider, Fischer-Tropsch process, (2002)
- [9] C. Maretto, V. Piccolo, Fischer-Tropsch process with a multistage bubble column reactor, (1998)
- [10] S. Schlüter, A. Steiff, P.-M. Weinspach, Heat transfer in two- and three-phase bubble column reactors with internals, *Chemical Engineering and Processing: Process Intensification* 34 (1995) 157–172
- [11] S. Schlüter, Modellierung und Simulation von Blasensäulenreaktoren, Ph.D. Thesis (1992).
- [12] C. Maretto, R. Krishna, Design and optimisation of a multi-stage bubble column slurry reactor for Fischer-Tropsch synthesis, *Catalysis Today* 66 (2001) 241–248
- [13] S. Berg, Zur Gasgehaltsverteilung und zum Verweilzeitverhalten der Gasphase in Blasensäulen mit längsangeströmten Rohrbündeleinbauten, Ph.D. Thesis (1993)

- [14] K. Bernemann, Zur Fluidodynamik und zum Vermischungsverhalten der flüssigen Phasen in Blasensäulen mit längsangeströmten Rohrbündeln, Ph.D. Thesis (1989)
- [15] A.A. Youssef, Fluid Dynamics and Scale-Up of Bubble Columns with Internals, Ph.D. Thesis (2010)
- [16] A. Forret, J.-M. Schweitzer, T. Gauthier, R. Krishna, D. Schweich, Liquid Dispersion in Large Diameter Bubble Columns, with and without Internals, *The Canadian Journal of Chemical Engineering* 81 (2003) 360–366
- [17] S. Nedeltchev, F. Möller, M. Schubert, Effect of Heat Exchanger Internals on the Main Transition Velocities in a Bubble Column, *Proceeding of the Third International Symposium on Multiscale Multiphase Process Engineering (MMPE)* (2017)
- [18] F. Möller, Y.M. Lau, T. Seiler, U. Hampel, M. Schubert, A study on the influence of the tube layout on sub-channel hydrodynamics in a bubble column with internals, *Chemical Engineering Science* 179 (2018) 265–283
- [19] Y.M. Lau, F. Möller, U. Hampel, M. Schubert, Ultrafast X-ray tomographic imaging of multiphase flow in bubble columns – Part 2: Characterisation of bubbles in the dense regime, *International Journal of Multiphase Flow* 104 (2018) 272–285
- [20] S. Nedeltchev, F. Möller, U. Hampel, M. Schubert, Flow Regime Transitions in a Bubble Column with Internals Based On a Novel Approach, *Chemical Engineering Journal Japan* (2018)
- [21] F. Möller, A. MacIsaac, Y.M. Lau, E. Schleicher, U. Hampel, M. Schubert, Advanced Analysis of Liquid Dispersion and Gas-Liquid Mass Transfer in a Bubble Column with Dense Vertical Internals, *Chemical Engineering Research and Design* 134 (2018) 575–588
- [22] F. Möller, R. Kipping, C. Lavetty, U. Hampel, M. Schubert, Two-bubble class approach based on measured bubble size distribution for bubble columns with and without internals, *Industrial & Engineering Chemistry Research* (2019)

- [23] Y. Ohki, H. Inoue, Longitudinal mixing of the liquid phase in bubble columns, *Chemical Engineering Science* 25 (1970) 1–16
- [24] F.C. Rubio, A.S. Mirón, M.C.C. García, F.G. Camacho, E.M. Grima, Y. Chisti, Mixing in bubble columns: a new approach for characterizing dispersion coefficients, *Chemical Engineering Science* 59 (2004) 4369–4376
- [25] P. Zehner, Modellbildung für Mehrphasenströmungen in Reaktoren, *Chemie Ingenieur Technik* 60 (1988) 531–539
- [26] J.B. Joshi, Axial mixing in multiphase contactors - a unified correlation, *Chemical Engineering Research and Design* (1980) 155–165
- [27] K. Ueyama, T. Miyauchi, Properties of recirculating turbulent two phase flow in gas bubble columns, *AIChE Journal* 25 (1979) 258–266
- [28] P. Gupta, B. Ong, M.H. Al-Dahhan, M.P. Dudukovic, B.A. Toseland, Hydrodynamics of churn turbulent bubble columns: gas-liquid recirculation and mechanistic modeling, *Catalysis Today* 64 (2001) 253–269
- [29] Y.T. Shah, S. Joseph, D.N. Smith, J.A. Ruether, Two-bubble class model for churn turbulent bubble-column reactor, *Industrial & Engineering Chemistry Process Design and Development* 24 (1985) 1096–1104
- [30] M.P. S. and Duduković Degaleesan, Liquid backmixing in bubble columns and the axial dispersion coefficient, *AIChE Journal* 44 (1998) 2369–2378
- [31] P. Gupta, M.H. Al-Dahhan, M.P. Dudukovic, B.A. Toseland, Comparison of single- and two-bubble class gas–liquid recirculation models — application to pilot-plant radioactive tracer studies during methanol synthesis, *Chemical Engineering Science* 56 (2001) 1117–1125
- [32] K. Shimizu, S. Takada, K. Minekawa, Y. Kawase, Phenomenological model for bubble column reactors: prediction of gas hold-ups and volumetric mass transfer coefficients, *Chemical Engineering Journal* 78 (2000) 21–28

- [33] F. Larachi, D. Desvigne, L. Donnat, D. Schweich, Simulating the effects of liquid circulation in bubble columns with internals, *Chemical Engineering Science* 61 (2006) 4195–4206
- [34] X. Guan, N. Yang, CFD simulation of pilot-scale bubble columns with internals: Influence of interfacial forces, *Chemical Engineering Research and Design* 126 (2017) 109–122
- [35] S. Degaleesan, S. Roy, S.B. Kumar, M.P. Duduković, Liquid mixing based on convection and turbulent dispersion in bubble columns, *Chemical Engineering Science* 51 (1996) 1967–1976
- [36] S. Degaleesan, M.P. Dudukovic, B.A. Toseland, B.L. Bhatt, A Two-Compartment Convective-Diffusion Model for Slurry Bubble Column Reactors, *Industrial & Engineering Chemistry Research* 36 (1997) 4670–4680
- [37] A. Döß, M. Schubert, A. Bieberle, U. Hampel, Non-invasive determination of gas phase dispersion coefficients in bubble columns using periodic gas flow modulation, *Chemical Engineering Science* 171 (2017) 256–270
- [38] M.J. Prince, H.W. Blanch, Bubble coalescence and break-up in air-sparged bubble columns, *AIChE J.* 36 (1990) 1485–1499
- [39] T.-J. Lin, J. Reese, T. Hong, L.-S. Fan, Quantitative analysis and computation of two-dimensional bubble columns, *AIChE J.* 42 (1996) 301–318
- [40] R. Higbie, The rate of absorption of a pure gas into a still liquid during short periods of exposure, *Transactions of the American Institute of Chemical Engineers* 31 (1935) 365–389
- [41] P. Rollbusch, M. Bothe, M. Becker, M. Ludwig, M. Grünewald, M. Schlüter, R. Franke, Bubble columns operated under industrially relevant conditions – Current understanding of design parameters, *Chemical Engineering Science* 126 (2015) 660–678

- [42] Y. Wu, B.C. Ong, M.H. Al-Dahhan, Predictions of radial gas holdup profiles in bubble column reactors, *Chem. Eng. Sci.* 56 (2001) 1207–1210
- [43] V.S. Vitankar, J.B. Joshi, A Comprehensive One-Dimensional Model for Prediction of Flow Pattern in Bubble Columns, *Chemical Engineering Research and Design* 80 (2002) 499–512
- [44] P. Zehner, Momentum, mass, and heat transfer in bubble columns: Flow model of bubble columns and liquid velocity, *Verfahrenstechnik* 16 (1982) 347–351
- [45] H. Riquarts, A physical model for axial mixing of the liquid phase for heterogeneous flow regime in bubble columns, *German Chemical Engineering* 4 (1981) 18–23
- [46] C. Wu, Heat Transfer and Bubble Dynamics in Slurry Bubble Column for Fischer-Tropsch Clea Alternative Energy, (2007)
- [47] Y. Liao, Development and validation of models for bubble coalescence and breakup /, *Wissenschaftlich-Technische Berichte / Helmholtz-Zentrum Dresden-Rossendorf*; (2013)
- [48] S.K. Majumder, *Hydrodynamics and Transport Processes of Inverse Bubbly Flow*, (Elsevier: 2016).
- [49] H. Zhao, W. Ge, A theoretical bubble breakup model for slurry beds or three-phase fluidized beds under high pressure, *Chemical Engineering Science* 62 (2007) 109–115
- [50] M. Jamialahmadi, M.R. Zehtaban, H. Müller-Steinhagen, A. Sarrafi, J.M. Smith, Fluid Flow Study of Bubble Formation Under Constant Flow Conditions, *Chemical Engineering Research and Design* 79 (2001) 523–532
- [51] F. Möller, C. Lavetty, E. Schleicher, M. Löschau, U. Hampel, M. Schubert, Hydrodynamics, mixing and mass transfer in a pilot-scale bubble column with dense internals, *Chemical Engineering Science* 202 (2019) 491–507
- [52] F. Möller, R. Kipping, E. Schleicher, M. Löschau, U. Hampel, M. Schubert, Comparative Hydrodynamic Analysis of Narrow and Pilot-Scale Bubble Columns with Internals, *Chemie Ingenieur Technik* (2019)

- [53] S. Wachi, Y. Nojima, Gas-phase dispersion in bubble columns, *Chemical Engineering Science* 45 (1990) 901–905
- [54] T. Wang, J. Wang, Y. Jin, Population balance model for gas- liquid flows: Influence of bubble coalescence and breakup models, *Industrial & engineering chemistry research* 44 (2005) 7540–7549
- [55] F. Lehr, M. Millies, D. Mewes, Bubble-Size distributions and flow fields in bubble columns, *AIChE Journal* 48 (2002) 2426–2443
- [56] M. Ishii, N. Zuber, Drag coefficient and relative velocity in bubbly, droplet or particulate flows, *AIChE Journal* 25 (1979) 843–855
- [57] N. Zuber, J.A. Findlay, Average volumetric concentrations in two-phase flow systems, *Journal of Heat Transfer* 87 (1965) 453–468
- [58] M.H.I. Baird, N.V.R. Rao, Axial mixing in a 15 cm diameter reciprocating plate bubble column, *The Canadian Journal of Chemical Engineering* 76 (1998) 370–378

Appendix

A.1 Breakup Kernel

Liao [47] propose

$$\Omega = \begin{cases} \sum_k \left(\frac{\tau_k - \tau_c}{\rho_l} \right)^{0.5} \frac{1}{d_j} & (\tau_k > \tau_c) \\ 0 & (\tau_k < \tau_c) \end{cases} \quad (\text{A-1})$$

as the final expression of the breakup frequency. The subscript k refers to the possible mechanisms leading to bubble breakup, namely, turbulence, laminar shear, eddy shear and interfacial slip. The destroying stress, τ_k , of the external flow is given as

$$\tau_k = \begin{cases} \tau_t = 0.5\rho_l\sqrt{2}(\varepsilon_d d_i)^{2/3} \\ \tau_s = \eta_l \dot{\gamma} \\ \tau_e = \eta_l \sqrt{\frac{\rho_l \varepsilon_d}{\eta_l}} \\ \tau_i = 0.5\rho_l u_{ri}^2. \end{cases} \quad (\text{A-2})$$

The critical stress, τ_c , that prevents the bubble from breaking up is calculated as

$$\tau_c = \max \left[6c_{fbv} \frac{\sigma}{d_i}, \frac{1}{\min(f_{bv}^{1/3}, (1 - f_{bv})^{1/3})} \frac{\sigma}{d_i} \right]. \quad (\text{A-3})$$

The subscript i in the equations above refers to the mother bubble. The subscript j indicates one of the two daughter bubbles, usually the smaller one. The turbulent energy dissipation rate, ε_d , is calculated as

$$\varepsilon_d = g u_g. \quad (\text{A-4})$$

The shear rate, $\dot{\gamma}$, was postulated by Shimizu et al. [32] as

$$\dot{\gamma} = \frac{du}{dr} \approx \frac{v_{1,c}}{D/2} = \frac{0.787(g D u_g)^{1/3}}{D/2}. \quad (\text{A-5})$$

Since the liquid velocity profile is determined in one of the sub-routines for the estimation of the flow pattern, the maximum liquid velocity, $v_{1,c}$, is directly taken from those calculations instead of using the given correlation described in A.3.

The bubble rise velocity of the parent bubble is calculated according to Equation 4. The auxiliary variable, c_{fbv} , depends on the breakup volume fraction, f_{bv} , and is defined as

$$c_{fbv} = f_{bv}^{2/3} + (1 - f_{bv})^{2/3} - 1. \quad (\text{A-6})$$

The breakup volume fraction, f_{bv} , is determined for every possible bubble diameter as a random value of an M-shape distribution as proposed by Zhao and Ge [49]. Accordingly, the size of the daughter bubble, d_j , can be estimated as

$$d_j = d_i \sqrt[3]{f_{bv}}. \quad (\text{A-7})$$

The unequal breakup can be regarded as an additional improvement compared to the unphysical equal-size breakup considered by Shimizu et al. [32]

A.2 Coalescence Kernel

The final expression for the coalescence frequency is defined by Liao [47] as

$$\Gamma(d_i, d_j) = \gamma \left(\begin{array}{l} \Pi S_{ij,t} u_{r,t} \lambda_t + S_{ij,s} u_{r,s} \lambda_s \\ + S_{ij,b} u_{r,b} \lambda_b + S_{ij,w} u_{r,w} \lambda_w \\ + S_{ij,e} u_{r,e} \lambda_e \end{array} \right). \quad (\text{A-8})$$

For the calculation of the modification factor, γ , the correlation

$$\gamma = \frac{\varepsilon_{g,\max_1}}{\varepsilon_{g,\max_1} - \varepsilon_g} \quad (\text{A-9})$$

of Wang et al. [54] is applied. The maximum gas holdup is defined as $\varepsilon_{g,\max_1} = 0,8$. The turbulent modification factor, Π , is determined as

$$\Pi = \exp \left[- \left(\frac{\varepsilon_{g,\max_2}^{1/3} - \varepsilon_g^{1/3}}{\varepsilon_g^{1/3}} \right)^2 \right] \quad (\text{A-10})$$

according to Lehr et al. [55], where the maximum gas holdup is defined as $\varepsilon_{g,\max_2} = 0,6$. The required cross-sectional areas for the collision are calculated by

$$S_{ij,t} = S_{ij,b} = S_{ij,s} = S_{ij,e} = \frac{\pi}{4} (d_i + d_j)^2 \quad (\text{A-11})$$

and

$$S_{ij,w} = \frac{\pi}{4} d_i^2. \quad (\text{A-12})$$

d_i and d_j refer to the diameters of the two colliding bubbles. Here, the larger bubble is labelled with the subscript i . The relative velocities between bubbles caused by different coalescence mechanisms are given as

$$u_{r,t} = \sqrt{2} \varepsilon_d^{1/3} (d_i^{2/3} + d_j^{2/3})^{1/2}, \quad (d_i + d_j) > \eta_k, \quad (\text{A-13})$$

$$u_{r,s} = 0.5(d_i + d_j)\dot{\gamma}, \quad (\text{A-14})$$

$$u_{r,b} = |u_{ri} - u_{rj}|, \quad (\text{A-15})$$

$$u_{r,w} = C_{35} u_{ri} C_D^{1/3}, \quad d_i \geq d_c, \quad (\text{A-16})$$

$$u_{r,e} = 0.5(d_i + d_j) \sqrt{\frac{\varepsilon_d}{\nu_l}}, \quad (d_i + d_j) \leq \eta_k. \quad (\text{A-17})$$

The Kolmogorov length scale, η_k , is defined as

$$\eta_k = \left(\frac{\nu_l^3}{\varepsilon_d} \right)^{0.25}. \quad (\text{A-18})$$

The critical bubble size, d_c , for the wake-entrainment is calculated according to

$$d_c = 4 \sqrt{\frac{\sigma}{g(\rho_l - \rho_g)}}. \quad (\text{A-19})$$

The turbulent energy dissipation rate, ε_d , is calculated using Eq. A-4 and the shear rate, $\dot{\gamma}$, is determined according to Eq. A-5, however considering the center-line liquid velocity obtained by the model of Vitankar and Joshi [43]. The bubble rise velocity for the respective bubble is calculated using Eq. 4. The coefficient C_{35} is considered constant (0.1) as proposed by Liao [47]. C_D refers to the drag coefficient, which is derived by the correlation of Ishii and Zuber [56] as

$$C_D = \frac{2}{3} E\ddot{o}^{0.5}. \quad (\text{A-20})$$

The dimensionless Eötvös number, $E\ddot{o}$, is defined as

$$E\ddot{o} = \frac{g(\rho_l - \rho_g)d_i^2}{\sigma}. \quad (\text{A-21})$$

Finally, the coalescence efficiency, λ_i , is calculated based on the film drainage model [38] according to

$$\lambda_t = \lambda_s = \lambda_b = \exp \left[-\frac{\rho_l^{0.5} r_{eq}^{1.5}}{4\sigma^{0.5}(d_i + d_j)} \ln \left(\frac{h_0}{h_f} \right) \max(u_{r,t}, u_{r,s}, u_{r,b}) \right], \quad (\text{A-22})$$

$$\lambda_e = \exp \left[-\frac{3\eta_l r_{eq}}{4\sigma} \sqrt{\frac{\varepsilon_d}{\nu_l}} \ln \left(\frac{h_0}{h_f} \right) \right], \quad (\text{A-23})$$

$$\lambda_w = 1. \quad (\text{A-24})$$

Initial and critical film thicknesses are h_0 and h_f . The equivalent bubble radius for two coalescing bubbles is determined as

$$r_{\text{eq}} = \frac{2r_i r_j}{r_i + r_j}. \quad (\text{A-25})$$

Using the equations above, the coalescence frequency can be calculated for every bubble pair. It should be noted that all given relations for breakup and coalescence are algebraic equations, which simplify the computation compared to other models.

A.3 Liquid Velocity Profile

The model of Vitanar and Joshi (2002) is based on the equations of motion for liquid and gas phase according to

$$\varepsilon_l \rho_l \frac{d\bar{u}_l}{dt} = -\varepsilon_l \bar{\nabla} p + \varepsilon_l \rho_l \bar{g} - \varepsilon_l \bar{f} - \nabla \varepsilon_l \bar{\tau}, \quad (\text{A-26})$$

$$\varepsilon_g \rho_g \frac{d\bar{u}_g}{dt} = -\varepsilon_g \bar{\nabla} p + \varepsilon_g \rho_g \bar{g} - \varepsilon_g \bar{f} - \nabla \varepsilon_g \bar{\tau}, \quad (\text{A-27})$$

where ε_l and ε_g are liquid and gas holdup, \mathbf{u} the phase velocities, \mathbf{g} the gravitational constant, \bar{f} the interface force, $\bar{\tau}$ the shear stress and $\bar{\nabla} p$ the pressure drop for a 3D system. For a 1D case (radial direction only), the upper equations can be simplified to

$$\frac{1}{r} \frac{d}{dr} (r \tau_{rz}) = -\frac{dp}{dz} - \varepsilon_l \rho_l g. \quad (\text{A-28})$$

The drift flux constants are determined using the drift flux model developed by Zuber and Findlay [57] according to

$$\frac{V_g}{\varepsilon_g} = C_0(V_g + V_1) + C_1, \quad (\text{A-29})$$

with

$$C_0 = \frac{\langle \varepsilon_g(\varepsilon_g u_g + V_1) \rangle}{\langle \varepsilon_g \rangle \langle (\varepsilon_g u_g + V_1) \rangle}, \quad (\text{A-30})$$

and

$$C_1 = \frac{\langle \varepsilon_g \varepsilon_1 V_s \rangle}{\langle \varepsilon_g \rangle}. \quad (\text{A-31})$$

The parameters C_0 and C_1 are the drift flux constants and represent the holdup profile nature and the bubble rise velocity. These parameters can be easily derived from gas holdup measurements as function of the superficial gas velocity.

To solve Eq. A-28, the radial holdup profile is implemented considering the radial holdup profile incorporating the wall holdup contributions according to

$$\varepsilon_g = \frac{m+2}{m} (\bar{\varepsilon}_g - \varepsilon_w)(1 - \xi^m) + \varepsilon_w. \quad (\text{A-32})$$

Utilizing Eq. A-32, the radial holdup profile can be incorporated into the motion Eq. A-28, which reads to

$$r\tau_{rz} = -\frac{dp}{dz}\frac{r^2}{2} - \rho_l \left(\frac{r^2}{2} - \frac{m+2}{m} [\bar{\varepsilon}_g - \varepsilon_w] \left[\frac{r^2}{2} - \frac{r^{m+2}}{(m+2)R^m} \right] - \frac{r^2}{2} \varepsilon_w \right) g. \quad (\text{A-33})$$

To eliminate dp/dz , the boundary conditions $\tau_{rz} = -\tau_w$ at $r = R$ are applied according to

$$-\frac{dp}{dz} = -\frac{2\tau_w}{R} + \rho_l(1 - \bar{\varepsilon}_g)g, \quad (\text{A-34})$$

$$\tau_{rz} = -(\mu_t + \mu_l) \frac{du_1}{dr} \quad (\text{A-35})$$

to describe the balance for the liquid velocity profile, which results in

$$\frac{du_1}{dr} = \xi R \frac{\tau_w}{\mu_t + \mu_l} \left[1 - \frac{R\rho_l g(\bar{\varepsilon}_g - \varepsilon_w)}{m\tau_w} (1 - \xi^m) \right]. \quad (\text{A-36})$$

The liquid velocity profile can be solved applying the boundary conditions at

$$\frac{du_1}{dr} = 0 \quad (\xi = 0) \quad (\text{A-37})$$

and

$$u_1 = 0 \quad (\xi = 1). \quad (\text{A-38})$$

Utilizing the energy dissipation [58] and further assumptions, described by Vitankar and Joshi [43], the turbulent kinematic viscosity can be calculated as

$$v_t = \frac{(XD)^{\frac{4}{3}} g^{\frac{1}{3}}}{6\sqrt{3}} \left(V_g - \frac{\bar{\varepsilon}_g V_1}{(1 - \varepsilon_g)} - \bar{\varepsilon}_g V_s \right)^{\frac{1}{3}} (1 + 2\xi^2)(1 - \xi^2). \quad (\text{A-39})$$

Specifying column dimensions, inlet conditions (D, V_g and V_1) as well as drift flux coefficients (C_0, C_1), the velocity profile can be calculated. Furthermore, the start value for the coefficient m of the holdup profile in Eq. A-36 is guessed. The slip velocity, V_s , is obtained from the drift flux constant according to C_1/ε_1 . The start value of the proportionality factor is defined as $X = 0.04$. Eventually, the velocity profile can be estimated with the only unknown being the wall shear stress. This parameter is selected to close the liquid phase balance

$$\int_{r=0}^R 2\pi\varepsilon_1 u_1 r dr = \frac{\pi}{4} D^2 V_1. \quad (\text{A-40})$$

If no liquid flow is induced, the right-hand side of the equation is set to zero. The value of X is evaluated with the energy balance according to

$$\begin{aligned} \frac{\pi}{4} D^2 \left(V_g - \bar{\varepsilon}_g \frac{V_1}{1 - \varepsilon_g} - \bar{\varepsilon}_g V_s \right) g \rho_1 L_D \\ = \rho_1 L_D \int_{r=0}^R 2\pi v_t \frac{du_1}{dr} \frac{du_1}{dr} r dr + \frac{\rho_1 L_D}{2D} \int_{r=0}^{\delta} 2\pi u_1^3 r dr. \end{aligned} \quad (\text{A-41})$$